Numerical analysis of the spatial range of the Kondo effect

C. A. Büsser,[1,*] G. B. Martins,[1] L. Costa Ribeiro,[2,3] E. Vernek,[4] E. V. Anda,[2] and E. Dagotto[5,6]
[1]*Department of Physics, Oakland University, Rochester, Michigan 48309, USA*
[2]*Departamento de Física, Pontifícia Universidade Católica do Rio de Janeiro, RJ, 22453-900, Brazil*
[3]*Centro Federal de Educação Tecnológica Celso Suckow da Fonseca (CEFET), RJ, Brazil*
[4]*Instituto de Física, Universidade Federal de Uberlândia, Uberlândia 38400-902, MG, Brazil*
[5]*Materials Science and Technology Division, Oak Ridge National Laboratory, Oak Ridge, Tennessee 37831, USA*
[6]*Department of Physics and Astronomy, University of Tennessee, Knoxville, Tennessee 37996, USA*
(Received 18 June 2009; revised manuscript received 25 November 2009; published 11 January 2010)

The spatial length of the Kondo screening is still a controversial issue related to Kondo physics. While renormalization-group and Bethe-Ansatz solutions have provided detailed information about the thermodynamics of magnetic impurities, they are insufficient to study the effect on the surrounding electrons, i.e., the spatial range of the correlations created by the Kondo effect between the localized magnetic moment and the conduction electrons. The objective of this work is to present a quantitative way of measuring the extension of these correlations by studying their effect directly on the local density of states (LDOS) at arbitrary distances from the impurity. The numerical techniques used, the embedded cluster approximation, the finite-U slave bosons, and numerical renormalization group, calculate the Green's functions in real space. With this information, one can calculate how the local density of states away from the impurity is modified by its presence, below and above the Kondo temperature, and then estimate the range of the disturbances in the noninteracting Fermi sea due to the Kondo effect, and how it changes with the Kondo temperature T_K. The results obtained agree with results obtained through spin-spin correlations, showing that the LDOS captures the phenomenology of the Kondo cloud as well.

DOI: 10.1103/PhysRevB.81.045111 PACS number(s): 73.23.Hk, 72.15.Qm, 73.63.Kv

I. INTRODUCTION

The physics of isolated impurities inside a Fermi sea has received considerable attention since it was experimentally shown that nanosystems composed by quantum dots display Kondo phenomena, very clearly reflected in its transport properties.[1] One signature of this effect is a narrow resonance, at the Fermi energy, in the local density of states (LDOS) of the impurity, with a width on the order of a characteristic energy, the so-called Kondo temperature, T_K. The transport properties of a nanoscopic structure in this regime are substantially affected by the Kondo resonance, as it creates an extra channel at the Fermi level through which the electrons can propagate. The energy $k_B T_K$ is also associated with antiferromagnetic correlations between the impurity and the conduction-electron spins in its neighborhood, favoring the emergence of a singlet ground state. These spins, localized in the impurity's vicinity, constitute a screening cloud of the localized impurity spin, known as the Kondo cloud. While most of the physics involved in this important effect is by now well established, the nature, structure, and extension of the Kondo cloud, and even its existence, is still, to some extent, controversial.[2,3] Theoretically, it is thought to be a crucial ingredient in helping to understand, for instance, the interaction between two nearby impurities, when one of them is sitting within the region of influence of the Kondo cloud of the other. From the experimental point of view, although it is thought that the extension of this characteristic cloud can reach very large values,[2] the properties of a system of impurities in metals seem to depend linear on the impurity concentration. This seems to indicate that the impurities do not see each other, although, based on the expected Kondo-cloud extension, they should. Moreover, there has not been any clear experimental evidence of it existence, with the exception of the electronic conductance measurements in quantum corrals.[4] For instance, in an ellipsoidal quantum corral, a Kondo peak produced by a magnetic atom located at one focus of the ellipse has an experimentally detectable spectral response in the other focus. This indicates a very peculiarly structured Kondo cloud, which, through the use of an scanning tunneling microscope (STM), can be experimentally analyzed.

The Kondo-cloud length can be estimated by considering that the mean life of the Kondo quasiparticles are related to the time scale $\tau_K \approx \hbar / k_B T_K$. Assuming that these quasiparticles propagate with the Fermi velocity v_F, then the Kondo screening length can be related to the quantity,[2]

$$R_K \approx \frac{\hbar v_F}{k_B T_K}. \tag{1}$$

Obviously, since all electrons whose energies fall within the Kondo peak will participate in the formation of the Kondo cloud, the quantity v_F is not well defined. Moreover, one may expect that the quasiparticles do not propagate with the bulk v_F but with a renormalized v^*, given by the presence of the impurity. From heavy fermion theory, we can estimate $v^* = k_F / m^*$, where m^* is the effective mass of the quasiparticle.[5] Therefore, Eq. (1) should provide inaccurate results for the screening length R_K. However, it should be expected to give the correct dependence with T_K and some plausible order of magnitude for its length.

From the theoretical point of view, this problem has been analyzed using different approaches.[6–11] The study of spin

properties, through the local susceptibility or the spatial spin-correlation function, has given significant contributions to the understanding of this phenomenon.[6,12,13] More closely related to our approach, the analysis of the conductance of a quantum dot embedded in a finite wire[2] or the persistent currents in a finite ring,[3] using renormalization arguments or density-matrix renormalization-group (DMRG) calculations, respectively, were proposed as a way of determining the Kondo cloud, as well.

More recently, a variational approach was proposed to study the propagation, from the impurity, of the local hole density.[14] In this work, it was possible to show that, in two and three dimensions, the extension of the Kondo cloud is on the order of a few Fermi wavelengths only, due to angular dispersion effects, such that R_K does not play a significant role in the physics of a system of impurities in either of these dimensions. This seems to explain the situation from the experimental point of view (as mentioned above), and thus the irrelevance of the Kondo cloud in most of the real systems studied. However, for one-dimensional (1D) systems,[14] the impurity-impurity interaction should be determined by the Kondo-cloud length R_K. This will have important consequences to the conductance properties, and therefore will have implications to the design of quantum-dot-integrated nanoscopic systems.

Motivated by this situation, we study the Kondo cloud in a one-dimensional system, focusing our attention on its electronic properties. The study of the propagation of the Kondo resonance, located at the vicinity of the Fermi energy, will shine light, for instance, into the transport properties of a quantum dot connected to leads where the distance from the dot to an STM tip is changed in a controlled and continuous way.[15] This will be experimentally similar to the transport properties studies of a system formed by a magnetic atom located in one focus of an elliptical quantum corral, as mentioned above, and can be experimentally implemented for a quantum dot connected into an infinite wire.

In the present work, we discuss the spatial behavior of the Kondo cloud by alternative means in an infinite one-dimensional system. Indeed, to estimate the cloud range, three different numerical techniques are used to track the effects of the impurity over the LDOS far away from the impurity. These effects are calculated above and below the Kondo temperature T_K, and their difference is used as a *finger print* of the extension of the Kondo cloud. The calculations are carried out using the embedded cluster approximation (ECA),[16,17] the finite-U slave-bosons mean-field approximation (FUSBMF),[18] and the numerical renormalization-group (NRG) method.[20]

The paper is organized as follows: in the next section (Sec. II), we present the model used and the methods to solve it. In Sec. III, we briefly describe the behavior of the LDOS, in real space, within the metal lead and define the function used to estimate R_K. In Sec. IV, the numerical results calculated using ECA, FUSBMF, and NRG are discussed and compared. In the last section, we present our conclusions. Finally, in the Appendix, we compare our approach and results with those presented in Ref. 8.

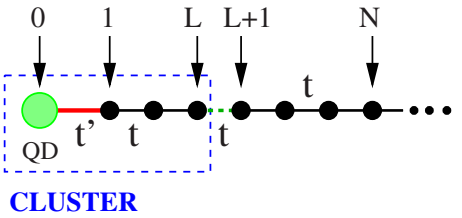

FIG. 1. (Color online) Schematics of the system used to determine the spatial extension of the Kondo cloud. The ED cluster (with a variable number of sites $L+1$, where the QD is numbered as site zero) is indicated by the dashed box. Note that the (integer) index $0 \leq N < \infty$ runs over all sites *inside and outside* the cluster. By applying the numerical methods employed in this work, the dressed (interacting) Green's function for all sites in the cluster is obtained (note that for FUSBMF and NRG, the cluster can be considered as just the impurity—see end of Sec. II B for details). A simple equation of motion procedure allows the calculation of the GF in any site of the semichain *outside* the cluster. With that, the effect of the Kondo screening over the noninteracting Fermi sea, the so-called Kondo cloud, can be probed at an arbitrary distance from the impurity.

II. SYSTEM AND NUMERICAL METHODS

In this work, we analyze a system composed by one Anderson impurity [representing, for example, a quantum dot (QD) or an adatom in a metal surface] coupled by a matrix element t' to a band (modeled by a semi-infinite noninteracting chain—from now on referred to as a semichain). This system is shown schematically in Fig. 1. This figure presents the system using the terminology appropriate for ECA, where a finite cluster has to be defined. However, as described in more detail below, we will show that, to calculate the Green's functions (GF) *outside* this cluster, when doing FUSBMF or NRG, the same terminology can be used, although there is no equivalent cluster definition in FUSBMF or NRG.

As shown in Fig. 1, N is an (integer) index that numbers the sites from zero to infinity, being the impurity [green (gray) circle], or QD, located at site $N=0$. The letter L is not an index and its meaning, related to ECA, but extended to the other methods, is explained below in Sec. II A 1.

The total Hamiltonian reads

$$H_T = H_{\text{imp}} + H_{\text{band}} + H_{\text{hybrid}} \tag{2}$$

with

$$H_{\text{imp}} = V_g \sum_{\sigma} n_{d\sigma} + U/2 \sum_{\sigma} n_{d\sigma} n_{d\bar{\sigma}}, \tag{3}$$

$$H_{\text{band}} = t \sum_{N=1\sigma}^{\infty} (c^{\dagger}_{N\sigma} c_{N+1\sigma} + c^{\dagger}_{N+1\sigma} c_{N\sigma}), \tag{4}$$

$$H_{\text{hybrid}} = t' \sum_{\sigma} (c^{\dagger}_{0\sigma} c_{1\sigma} + c^{\dagger}_{1\sigma} c_{0\sigma}), \tag{5}$$

where $c^{\dagger}_{0\sigma}$ creates an electron at the impurity, $c^{\dagger}_{N\sigma}$ creates an electron at the site N of the lead, and $n_{d\sigma}=c^{\dagger}_{0\sigma}c_{0\sigma}$ is the number operator at the impurity. The first two terms of H_T

represent the Hamiltonian of the impurity and the noninteracting band, respectively, and the last term is the hybridization between them. An important quantity for this system is the broadening of the impurity level $\Gamma=2\pi t'^2\rho_{\text{lead}}(E_F)$, where $\rho_{\text{lead}}(E_F)$ is the LDOS of the first site in the semichain at the Fermi energy E_F.

Note that the model displayed in Fig. 1 [and also denoted in Eqs. (2)–(5)], i.e., an impurity connected to one end of a semi-infinite chain, can be obtained from a model where the impurity is *embedded* into an infinite chain. Indeed, the first model (plus, a noninteracting semi-infinite chain) is obtained from the second through a symmetric/antisymmetric transformation of the fermionic creation and annihilation operators for the sites of the infinite chain. This canonical transformation has been widely used (e.g., see Ref. 17, and references therein). In this paper, we will concentrate our attention on the electron-hole symmetric point ($V_g=-U/2$), although the results can be generalized to an arbitrary value of gate potential. As mentioned in Sec. I, we want to estimate the extension of the Kondo cloud, and its dependence on U/Γ, by analyzing the LDOS calculated through the local GF. To calculate the GF, we will use the ECA, the FUSBMF, and the NRG methods, which are briefly described next.

At the end of this section we will describe how the LDOS in a site N far away from the impurity is calculated using the equation of motion (EOM) method. Note that the EOM method described in Sec. II B does not depend on the method used to calculate G^{σ}_{dd}; any of the three methods described below provide essentially the same kind of input for the EOM procedure.

A. Numerical methods

1. Embedded cluster approximation method

The ECA method has been developed to treat localized impurity systems consisting of a many-body interacting region weakly coupled to noninteracting conduction bands. The approach is based on the idea that the many-body effects of the impurity are local in character (the Kondo cloud, for instance). With this in mind, we proceed in three steps: first, out of the complete system (the impurity plus a noninteracting band, described by a tight-binding Hamiltonian), one isolates a cluster consisting of the impurity plus their L nearest-neighboring sites in the tight-binding semichain. This cluster, with a variable size $L+1$, as it includes the impurity, is shown in Fig. 1 by dashed lines. The first site outside the cluster is labeled $N=L+1$ (remember that N is an index, as opposed to a number of sites). Most of the many-body effects are expected to be confined to this cluster.

The second step of the method consists in exactly diagonalizing the cluster, using, for example, the Lanczos method,[21] and calculate all the GFs. Finally, in the third step, the cluster is embedded into the rest of the tight-binding semichain using a Dyson equation.[16,17]

Being $g_{i,j}$ a cluster GF that propagates an electron from site i to j and g_{L+1} the GF of the first site out of the cluster ($N=L+1$), the Dyson equation to calculate a dressed (by the presence of the semichain) GF for sites inside the cluster can be written as

$$G_{i,i} = g_{i,i} + g_{i,L}tG_{L+1,i}, \tag{6}$$

$$G_{L+1,i} = g_{L+1}tG_{L,i}. \tag{7}$$

Note that the hopping parameter t in Eq. (6) corresponds to the broken link shown by a dashed line in Fig. 1. This matrix element has the same value as all the other hopping parameters within the chain. Properties such as conductance through the impurity and its LDOS, for example, can be obtained by solving this set of equations (for more details, see Refs. 16 and 17).

2. Finite-U slave-bosons mean-field approximation

The slave-boson mean field is a method proposed originally to treat the problem when the Coulomb repulsion U is the larger quantity. The double occupancy is excluded from the Hilbert space with the help of projectors-bosons operators. After taking a mean field in the boson operators, the many-body Hamiltonian is mapped into an effective one-body Hamiltonian that can be solved exactly.[19]

The FUSBMF approach is an extension of the usual slave-boson mean field in order to treat problems with finite U.[18] The first step is to enlarge the Hilbert space by introducing a set of slave boson operators $\hat{e}$, $\hat{p}_\sigma$, and $\hat{d}$, and replacing the creation ($d^\dagger_\sigma$) and annihilation ($d_{i\sigma}$) operators in the Hamiltonian by $d^\dagger_\sigma\hat{z}^\dagger_\sigma$ and $\hat{z}_\sigma d_{i\sigma}$, respectively. Following Kotliar and Ruckenstein,[18] the operator z takes the form[18]

$$\hat{z}_\sigma = [1-\hat{d}^\dagger\hat{d}-\hat{p}^\dagger_\sigma\hat{p}_\sigma]^{1/2}[\hat{e}^\dagger\hat{p}_\sigma+\hat{p}^\dagger_{\bar{\sigma}}\hat{d}]\times[1-\hat{e}^\dagger\hat{e}-\hat{p}^\dagger_{\bar{\sigma}}\hat{p}_{\bar{\sigma}}]^{1/2}. \tag{8}$$

Notice that the bosonic operators $\hat{d}$ and $\hat{d}^\dagger$ do not carry spin index. The enlarged Hilbert space is then restricted to the physically meaningful subspace by imposing the constraints

$$\hat{P} = \hat{e}^\dagger\hat{e} + \sum_\sigma \hat{p}^\dagger_\sigma\hat{p}_\sigma + \hat{d}^\dagger\hat{d} - 1 = 0 \tag{9}$$

and

$$\hat{Q}_\sigma = n_{d\sigma} - \hat{p}^\dagger_\sigma\hat{p}_\sigma - \hat{d}^\dagger\hat{d} = 0. \tag{10}$$

Both constraints are included into the Hamiltonian through Lagrange multipliers $\lambda^{(1)}$ and $\lambda^{(2)}_\sigma$. The constraint described by Eq. (9) forces the dots to have empty, single, or double occupancy only, while the constraint of Eq. (10) relates the boson with the fermion occupancies. In the mean-field approximation, we replace the boson operators $\hat{e}$, $\hat{p}_\sigma$, and $\hat{d}$ (and their Hermitian conjugates) by their thermodynamical expectation values $e\equiv\langle\hat{e}\rangle=\langle\hat{e}^\dagger\rangle$, $p_\sigma\equiv\langle\hat{p}_\sigma\rangle=\langle\hat{p}^\dagger_\sigma\rangle$, and $d\equiv\langle\hat{d}\rangle=\langle\hat{d}^\dagger\rangle$. These expectation values, plus the Lagrange multipliers, constitute a set of parameters to be determined by minimizing the total energy $\langle H\rangle$. In principle, it is necessary to have a set of seven self-consistent parameters. Once again, as in the infinite U case, the problem was reduced to a one-body Hamiltonian whose energy can be minimized easily. The quantity we need to calculate is the Green's function at the impurity, around the Fermi level. Thus,

$$G_{dd}^{\sigma} = \langle\langle z_{\sigma} d_{\sigma}; d_{\sigma}^{\dagger} z_{\sigma}^{\dagger} \rangle\rangle, \tag{11}$$

which is the propagator that carries the correct weight of the Kondo resonance.

In Sec. II B it will be shown how to calculate the GF in the lead's sites using G_{dd}^{σ} as an input.

3. Numerical renormalization-group approach

The NRG method was originally proposed by Wilson to study magnetic impurity problems.[20] Initially, it was applied to the Kondo Hamiltonian, and later extended to the Anderson model.[22] It can be shown that for these two models, at low temperatures, the states close to the Fermi level (i.e., with the lowest-energy contribution) are the most relevant. Therefore, perturbation theories are not the most adequate approach to these problems. As a brief description of the method (a full detailed description can be found in Refs. 20 and 23), we present the two main steps in the implementation of the method.[23] The first one consists in sampling the energy interval of the conduction band by a set of logarithmically decreasing energy intervals $[x_N, x_{N-1}]$, defined by $x_N = \pm D\Lambda^{-N}$, where Λ is the discretization parameter and D is the half width of the conduction band. Then, from each interval, only one representative energy value is kept (chosen according to a well-defined criterion, see Ref. 23 for details). The total number of representative energies, one from each interval, results in the set of discrete energies that couples to the impurity. After these two basic steps, the total Hamiltonian is mapped into a semi-infinite chain, commonly known as *Wilson-chain*, where each site of the chain corresponds to an energy scale in the logarithmically discretized conduction band, with the impurity sitting at its first site. It is important to notice that the t_n couplings, between adjacent sites n and $n+1$, decrease, away from the impurity, as $\Lambda^{-n/2}$. The final form for the Hamiltonian in the NRG framework is

$$H = \lim_{N\to\infty} \Lambda^{-(N-1)/2} H_N, \tag{12}$$

where

$$H_N = \Lambda^{(N-1)/2} \Bigg[H_{\text{imp}} + t' \sum_{\sigma} (d_{\sigma}^{\dagger} c_{0\sigma} + \text{H.c.}) + \sum_{n=0,\sigma}^{N} \epsilon_n c_{n\sigma}^{\dagger} c_{n\sigma} + \sum_{n=0,\sigma}^{N-1} t_n (c_{n\sigma}^{\dagger} c_{n+1\sigma} + \text{H.c.}) \Bigg], \tag{13}$$

where d_{σ} annihilates an electron with spin σ at the impurity and $c_{n\sigma}$ annihilates one at site n in the semi-infinite chain (indexed from $n=0$ to N).

Note that an explicit analytical expression for t_n in Eq. (13) cannot be obtained for a band of arbitrary shape. For the present problem, where a semielliptical band is used, we are forced to calculate the t_n numerically.[24] The hoppings t_n that define the Wilson-chain must not be confused with the matrix elements t of the real-space chain, shown in Fig. 1. The elements t_n correspond to the band obtained after the logarithmic discretization of the real-space chain. It can be shown that when $\Lambda \to 1$, the hoppings $t_n \to t$.[23]

The second important step consists in solving numerically the resulting Hamiltonian given by Eq. (12). To this end, we start with a system consisting of the isolated impurity, described by the Hamiltonian H_{imp}. Then, the subsequent sites are added one by one. This procedure generates a sequence of Hamiltonians H_N, which are solved as follows: at a given iteration N the Hamiltonian H_N is diagonalized numerically. The eigenvectors and the corresponding eigenvalues are obtained. Next, a new site $N+1$ is added. This is done by enlarging the current Hilbert space (associated to iteration N) through a tensorial product of its elements with the states of the site being added in the next iteration. This process results in an exponential growth of the dimension of the Hilbert space of successive iterations. Due to computational constraints, it is necessary to truncate the Hilbert space at each iteration, after it reaches a certain size. The NRG truncation criterion is to keep only the M lowest-energy states of H_N (typically, $M=1000$), and neglect the higher-energy spectrum.

The process of adding a single site to H_N is repeated until the system reaches the strong-coupling fixed point. When this fixed point is reached, H_N and H_{N+2} have the same eigenvalues.[20]

The sequence of iterations described above can be thought of as a RG process. Adding one site to the chain, and obtaining the new low-energy spectra, can be understood as an RG transformation $\mathcal{R}$ that maps the Hamiltonian H_N into a new Hamiltonian $H_{N+1} = \mathcal{R}(H_N)$, which has the same form as H_N. Once the fixed points are obtained, the static and dynamic properties, as well as temperature effects, can be calculated.[20,23] In particular, we are interested in the local GF at the impurity.

At this point it is worth to remind the reader that the information about the high-energy dynamics is not accurately taken into account since the high-energy spectra is partially neglected after the truncation.

All the NRG data presented in this work was calculated with $\Lambda = 2.5$ and keeping the $M=1000$ lower-energy states in each iteration. To calculate the LDOS at the impurity, the delta functions were broadened using logarithmic Gaussians with a $b=0.6$ factor (see Ref. 23).

Finally, we want to stress, once again, the difference between the real-space semi-infinite chain and the Wilson-chain. The first one, shown in Fig. 1, has all the hopping terms equal to t. The Wilson-chain is just used to calculate the GF at the impurity, and it is obtained after the discretization of the real-space chain. With the impurity propagator, obtained from NRG, the LDOS at any site of the real-space chain can be calculated, as explained below.

B. LDOS away from the impurity: Equation of motion

In this section, we will explain how to calculate the LDOS at any site of the semichain, which models the electron reservoir. Note that, for all numerical methods used in this work, once the dressed GF is known at the impurity (and, in the case of ECA, for all the other sites of the cluster), a procedure based on the construction of a Dyson equation, through the use of a sequence of equation of motion, can yield the dressed GF for any site in the tight-binding semichain, no matter how far away from the impurity. This can be

most easily understood in the case of ECA, as this idea is built into the very core of the method. Indeed, ECA allows us to calculate not just the LDOS in all the sites of the cluster but also in all the sites in the rest of the semi-infinite tight-binding chain used to represent the lead. An important fact that we want to remark regarding ECA is that the embedding procedure results in a *feedback* of the leads into the central region but also reciprocally. The physics under study does not need to be restricted to entirely occurring within the exactly solved region. I.e., many-body effects taken into account *exactly* inside the exactly diagonalized (ED) cluster are propagated, by the Dyson equation, into the electron reservoir (the semichain), which now does not have anymore the LDOS of a noninteracting system. It is important to remark, as will be clearly explained shortly, that the change in the LDOS in the semichain from tight binding to many body lies at the core of the method used in this work to estimate the range of the Kondo cloud. One added benefit of the procedure to be described below is that the physics of the Kondo effect *at* the impurity (the Kondo resonance) does not need to be calculated with ECA for the EOM procedure to work. In the present work, it is also calculated with FUSBMF and NRG.

To calculate the dressed propagators at any site of the semichain, we write down the EOM of the local propagators at a site M. In the case of ECA, the site M must be outside the cluster, i.e., $M \geq L+1$ (see Fig. 1). This restriction does not apply to FUSBMF or NRG, where the equivalent to the ECA cluster can be considered to be *just* the impurity. A brief description of the EOM method can be found in Ref. 25. To simplify the notation, in what follows we will ignore the spin index σ. The set of equations to solve, in order to calculate $G_{M,M}$, is given by

$$G_{M,M} = g_0 + g_0 t G_{M-1,M} + g_0 t G_{M+1,M}, \tag{14}$$

$$G_{M+1,M} = \tilde{g}_{sc} t G_{M,M}, \tag{15}$$

$$G_{M-1,M} = G_{M,M-1} = g_0 t G_{M-1,M-1} + g_0 t G_{M+1,M-1}, \tag{16}$$

$$G_{M+1,M-1} = \tilde{g}_{sc} t G_{M,M-1}, \tag{17}$$

where $g_0 = 1/\omega$ is the atomic GF at site M and $\tilde{g}_{sc}$ is the bare propagator for the rest of the semichain starting at the site $M+1$ and is given by

$$\tilde{g}_{sc} = \frac{\omega \pm \sqrt{\omega^2 - 4t^2}}{2t^2}. \tag{18}$$

In Eq. (16), we used explicitly the equivalence between $G_{M-1,M}$ and $G_{M,M-1}$. This is only valid if the hopping parameters t are real (e.g., no magnetic field inside the chain, although a more general EOM, involving a magnetic field, can also be found).

Solving this set of equations, we obtain

$$G_{M,M} = \frac{g_0 + \dfrac{g_0 t g_0 t}{1 - g_0 t^2 \tilde{g}_{sc}} G_{M-1,M-1}}{1 - g_0 t^2 \tilde{g}_{sc}}. \tag{19}$$

Note that the GF at the site M can be calculated through the GF at $M-1$. Note that the equation above clearly indicates that, to calculate the dressed GF at site M, the only many-body information needed is the dressed GF at site $M-1$. This fact automatically defines a procedure to find the propagator at any site in the semichain. Note that Eq. (19) is defined for a site, within the semichain (i.e., $M \geq 2$), that is connected to both adjacent sites by a matrix element t. Thus, this still leaves us with the task of calculating $G_{1,1}$. To calculate the correct propagator at site 1, we have to rewrite Eqs. (14)–(17), in order to obtain $G_{1,1}$ as a function of $G_{0,0}$, without overlooking that the hopping between sites 0 and 1 is t', not t.

For FUSBMF and NRG, we start with the GF calculated at the impurity, i.e., $G_{0,0}$. Using the EOM method, we calculate the propagator at the first site of the chain, $G_{1,1}$. Then, using Eq. (19), the propagator $G_{M,M}$ can be calculated at any site. The procedure for the ECA method is slightly different, as in ECA all the dressed propagators inside the ED cluster are calculated already within the method. Therefore, in ECA, the EOM procedure starts at site $L+1$ (see Fig. 1), using Eq. (19), where $G_{L,L}$ is an input from the ECA calculations. In that case, there is no special procedure to calculate $G_{1,1}$.

Once $G_{M,M}$ is calculated for the desired site M, the LDOS can be calculated as

$$\varrho_M(\omega) = \frac{-1}{\pi} \mathrm{Im}[G_{M,M}]. \tag{20}$$

As we are using the same procedure to find the LDOS away from the impurity for three very diverse numerical methods (ECA, FUSBMF, and NRG), some explanation about the adopted terminology is necessary, so that the same term, with slightly different meanings, can be unambiguously used throughout the paper. As explained in Fig. 1, in ECA, *cluster* means a variable size finite group of sites (including the impurity), which is exactly diagonalized and embedded (as explained above). In this paper, the ECA *cluster* contains up to $L+1=10$ sites (i.e., the impurity plus up to $L=9$ tight-binding sites). For sites $N \geq L+1$, the LDOS will be found through the EOM method, as described above. On the other hand, an FUSBMF or an NRG *cluster*, given the very nature of both methods, contains just the impurity itself (therefore, $L=0$, see Fig. 1). Because of that, there is a slight difference to the application of the EOM method to these last two methods, viz., $G_{1,1}$ has to be calculated first, and then all the other $G_{i,i}$ are calculated by using Eq. (19) in sequence, as explained above.

III. LOCAL DENSITY OF STATES WITHIN THE METAL HOST

Using the FUSBMF approximation, we can obtain analytically self-consistent expressions for the GF, and then the LDOS. The local GF is also obtainable within NRG, i.e., the

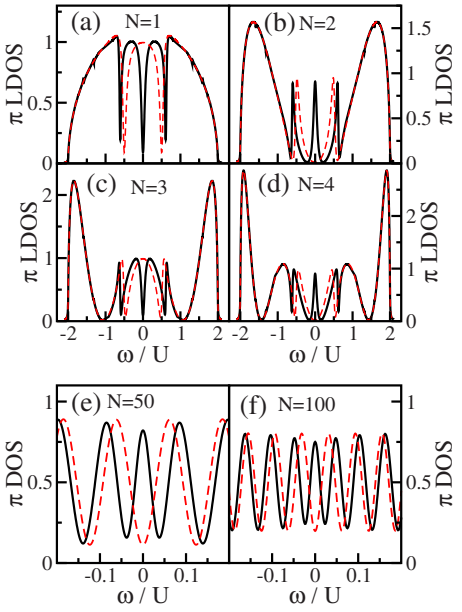

FIG. 2. (Color online) (a)–(f) The LDOS for sites $N=1$, 2, 3, 4, 50, and 100 (see Fig. 1), calculated by ECA for a cluster with $L=3$ (note that the impurity is located at $N=0$). Solid (black) curves show the LDOS at $T=0$ for $V_g=-U/2$, $U=t$, and $t'=0.3t$ while dashed (red) curves show results for $T>T_K$ and the same values for V_g, U, and t'. An imaginary part $\nu=0.001$ was used to regularize the LDOS. Note that the LDOSs for the first three panels were calculated using ED, in contrast to the ones for the last three panels, which were calculated using the EOM method described in the text. The LDOS for the first three sites ($N=1$, 2, and 3) was also calculated with EOM and, as expected, there was a very good agreement between the results obtained with the two different methods. Note that the small value used for L (=3) was in order to avoid a large number of dips in the solid curves [number of dips equals $L+1$; check, for example, solid curve in panel (a)]. Nonetheless, the qualitative form of the curves is not affected by the choice of L.

LDOS *at* the impurity can be found with very good accuracy, and, as explained in Sec. II B, the GF (and therefore the LDOS) can be calculated within the semichain that models the noninteracting band. The same is valid for ECA, despite the distinctions drawn above between ECA, on the one hand, and FUSBMF and NRG, on the other hand.

In Fig. 2, we show the LDOS for several different sites within the noninteracting semichain ($N>0$), calculated by ECA. The parameters used are $U=t$ and $\Gamma=0.1t$, and the gate potential is set at the electron-hole symmetric point ($V_g=-U/2$). The LDOS for sites *outside* the cluster were obtained through the procedure described in Sec. II B. The LDOS at zero temperature is shown in solid lines. In dashed lines, for comparison, we show the LDOS when the impurity is out of the Kondo regime ($T>T_K$). In order to obtain a solution for $T>T_K$, we use the Hubbard-I approximation,[26] which eliminates the spin correlations between the impurity and the leads and, as a consequence, all the low-energy excitations responsible for the Kondo physics. This approximation is equivalent to performing an ECA calculation where the cluster contains just the impurity ($L=0$ in Fig. 1, i.e., the atomic solution). To understand the results in Fig. 2, it is instructive to analyze the results shown in Fig. 3, where, in

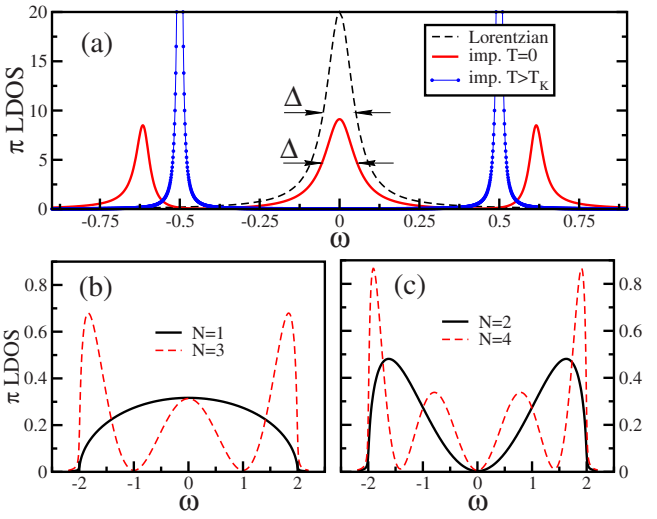

FIG. 3. (Color online) (a) LDOS for site $N=0$, where the impurity is located (see Fig. 1), calculated by ECA. Solid line shows LDOS for $V_g=-U/2$, $U=t$, and $t'=0.3t$ while in dashed lines, results are shown for $T>T_K$ and the same parameter values for V_g, U, and t'. An imaginary part $\nu=0.001$ was used to regularize the LDOS. The dashed (black) curve displays an example of the normalized Lorentzian used to convolute the data in Eq. (22). (b) LDOS for the first and third sites of a noninteracting semichain with bandwidth $D=4t$. (c) Same as (b) but now for the second and fourth sites.

panel (a) it is shown the LDOS at the impurity, for $T=0$ [(red) solid line) and for $T>T_K$ [(blue) dotted curve], and in panels (b) and (c) the LDOS of the first four edge sites of an isolated noninteracting semichain. The results shown in Fig. 2 [panels (a)–(d)] display essentially the *hybridization* between the LDOS of the impurity [panel (a) in Fig. 3] and the LDOS of the sites in the semichain [panels (b) and (c) in Fig. 3], once the impurity is coupled to the semichain. The solid (black) curve shows the LDOS for $T=0$ while the dashed (red) curve shows the LDOS for $T>T_K$, at the first four sites in the semichain, after it couples to the impurity. This hybridization can be described in a simple way: a peak in the LDOS of the impurity [Fig. 3(a)], centered at ω_p, will generate either a resonance or an antiresonance (at ω_p) in the LDOS of a semichain site when the impurity couples (hybridizes) to the semichain. On the one hand, a resonance (a peak) will result if the semichain's LDOS, in one specific site, vanishes at ω_p. On the other hand, an antiresonance (a dip) results when the site's LDOS at ω_p is finite. This resonance/antiresonance site to site oscillation effect in the LDOS will have important consequences in the next section. Our interest is to be able to distinguish the effect caused over the semichain's LDOS, far away from the impurity, by the presence ($T<T_K$) or absence ($T>T_K$) of a resonance at the Fermi energy (the Kondo peak) in the LDOS *at* the impurity [compare the solid and dotted curves in Fig. 3(a)]. The extent to which this hybridization effect can spread away from the impurity will be used as a measure of the extent of the Kondo cloud.

Figure 2 clearly displays this kind of hybridization effect, as described above. Indeed, if one concentrates the attention

on the features close to the Fermi energy ($\omega=0$) in the different panels in Fig. 2, one sees that the difference between the LDOS curves below T_K (solid) and above T_K (dashed) is quite marked, and owes its origin to the presence of the Kondo peak at the impurity below T_K. By using the Lorentzian shown in Fig. 3 (dashed line) to restrict ones attention to the immediate neighborhood of the Fermi energy, by convoluting it with the *difference* between the solid and dashed curves in Fig. 2, one expects to extract the essence of the influence of the impurity, when in the Kondo regime, over the Fermi sea. One can picture the change from the solid to the dashed curve, say, in site 50 [panel (e)], as that occurring in the LDOS away from the impurity when the temperature is lowered below T_K. Panel (f), where there is very little difference between both curves, shows that the impurity, in a Kondo regime, has a spatially limited influence over the Fermi sea. It is one of the aims of this paper to understand how this influence depends on the sole energy scale of the Kondo effect, i.e., the Kondo temperature T_K.

IV. CLOUD EXTENSION FUNCTION

As mentioned in Sec. I, considering that the width of the Kondo resonance in the LDOS at the impurity, Δ, is proportional to T_K, we expect that

$$R_K \approx \frac{1}{\Delta}, \tag{21}$$

In this section, we will estimate the screening length R_K by evaluating the *distortion* in the LDOS, produced by the Kondo resonance at the impurity, in sites N arbitrarily far away from the impurity. The distortion produce in site N will be quantified by the absolute value of the function $F(N)$, as defined by

$$F(N) = \int_{-\infty}^{\infty} [\varrho_N^K(\omega) - \varrho_N^{NK}(\omega)] L_\Delta(\omega) d\omega, \tag{22}$$

where ϱ_N^K (ϱ_N^{NK}) is the local density of states at the site N in the Kondo regime (out of Kondo), and L_Δ is the Lorentzian distribution of width Δ [dashed curve in Fig. 3(a)]. Note that the distance to the impurity is given by $r=Na$, where a is the lattice parameter. To evaluate ϱ_N^{NK}, we applied the EOM procedure to the Hubbard-I solution for the impurity's GF [where the dotted line in Fig. 3(a) shows the negative of its imaginary part]. It is important at this point to remind the reader that all the calculations here were done at $V_g=-U/2$ (i.e., at the particle-hole symmetric point).

Note that, for a site far away from the impurity, where the many-body effects are not important, ϱ_N^K must be equal to ϱ_N^{NK}, thus $F(N)\approx 0$. This can be seen in the last panel of Fig. 2. $F(N)$ will be used to find a length scale beyond which the presence of the impurity is not relevant any more. We will call $F(N)$ the *cloud extension function*. We define the extension function in this form due to several reasons. First, because this definition associates this function to the conductance, a quantity that can be experimentally measured. It is clear that charge transport involves a local density of states integrated over a frequency window around the Fermi level with a width given by the applied external bias, which can be adjusted to be proportional to an experimental estimate of the Kondo temperature. Regarding this point, and for the sake of clarity, it is important to stress that the function $[\varrho_N^K(\omega) - \varrho_N^{NK}(\omega)]$, appearing in Eq. (22), is different from the quantity calculated in most studies of the Kondo-cloud problem.[2,6,7] (In reality, this point will be expanded in detail in the Appendix). Here, ϱ_N^{NK} corresponds to the local density of states above the Kondo temperature, and *not* to the local density of states of the system when the magnetic impurity is removed, a situation that is not experimentally feasible. Moreover, the Lorentzian convolution in the definition of $F(N)$ eliminates the trivial $1/N$ dependence of the Friedel oscillations, and, in reality, the oscillations themselves, keeping only the nontrivial Kondo physics. As will be shown in the Appendix, this happens because the convolution with a Lorentzian (which has smooth tails) removes the abrupt discontinuity at $\omega=\pm\Delta/2$ [see Eq. (A2)], that causes the oscillations. A similar role is played by temperature in any real experimental situation, even for $T \ll T_K$, i.e., the same *smoothing* effect played by the Lorentzian in Eq. (A2), is played by temperature in the Fermi function in Eq. (A1): both of them tend to suppress the Friedel oscillations. More importantly from a conceptual point of view, as will be rigorously shown in this section through numerical results,[27] $F(N)=F(N/R_K)$ is a universal function of N/R_K and contains, through its exponential dependence, the information about the extension and the simple structure of the Kondo cloud in a 1D system. As it will be shown in the Appendix, by substituting the Lorentzian by a square distribution [see Eq. (A2)], with the Fermi level at the middle of the band, monochromatic Friedel oscillations are restored, together with the two asymptotic behaviors discussed in Ref. 8.

As already mentioned, to calculate ϱ_N^K, we will use ECA, FUSBMF, and NRG. In Fig. 4(a), it is shown the absolute value of the cloud extension function, $|F(N)|$, calculated with ECA, as a function of N, for $U=t$, $\Gamma=0.1t$, and for several values of L (note that the vertical axis has a logarithmic scale). The scatter plots show the data obtained from Eq. (22) for some selected values of N, for different cluster sizes L (see legend). We find that the behavior of $|F(N)|$, for all values of L used, is a decaying exponential (the correlation factor, when fitting the curves with an exponential, was exactly 1 for all values of L),

$$|F(N)| = A_0 \exp(-N/R_K), \tag{23}$$

where R_K marks the distance from the impurity where the value of $|F(N)|$ has fallen by $1/e$, in comparison to its value at the impurity ($N=0$). The solid lines in panel (a) show the result of fitting each set of data with Eq. (23). In the inset of Fig. 4(a), it can be observed that $F(N)$ oscillates between positive and negative values for successive N.[28] This is a direct consequence of the resonance/antiresonance oscillation in the LDOS discussed in the previous section. The extrapolation of R_K to an "infinite" ECA cluster ($1/L\to 0$) is explained in detail next.

As mentioned already, each curve in Fig. 4(a) (from $L=1$ to $L=9$) is fitted using Eq. (23). Therefore, a value for $R_K(L)$ is found for each cluster size used in ECA ($1\leq L$

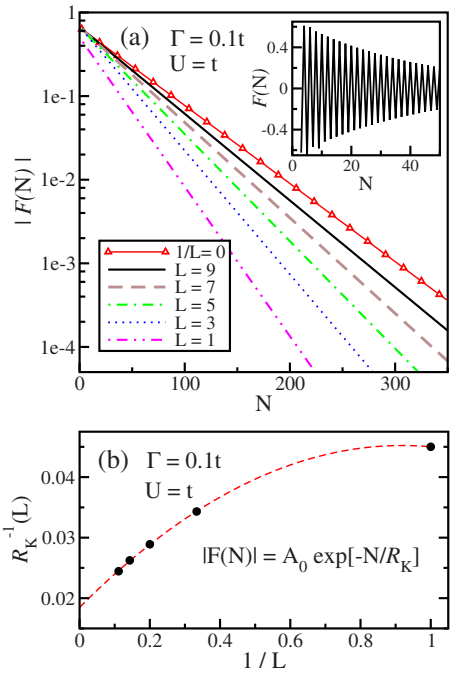

FIG. 4. (Color online) (a) Main panel: Absolute value of the cloud extension function, $|F(N)|$, calculated by ECA as a function of the semichain site N for several different cluster sizes ($L=1-9$, in steps of 2—see legend). The parameter values are $U=t$ and $\Gamma=0.1t$. Note that L is the number of nearest-neighboring sites to the impurity within the cluster solved exactly in ECA. The curves shown are the data obtained through Eq. (22). Fits to these data (not shown), for each value of L, using Eq. (23), result in exactly the same curves as the ones shown. It is clear that the data for each different cluster size decays exponentially with N (notice the logarithmic scale in the vertical axis). The open (red) triangles curve shows the extrapolation of $|F(N)|$ to the thermodynamical limit, as describe in detail in the text. The inset shows the site to site oscillations of $F(N)$, as well as the exponential decay, now with a linear scale for the vertical axis. (b) ECA extrapolation to the thermodynamical limit [dashed (red) curve], as described in the text, of the R_K data [solid (black) dots] obtained from the fittings for each different L curve shown in panel (a), as explained in the text.

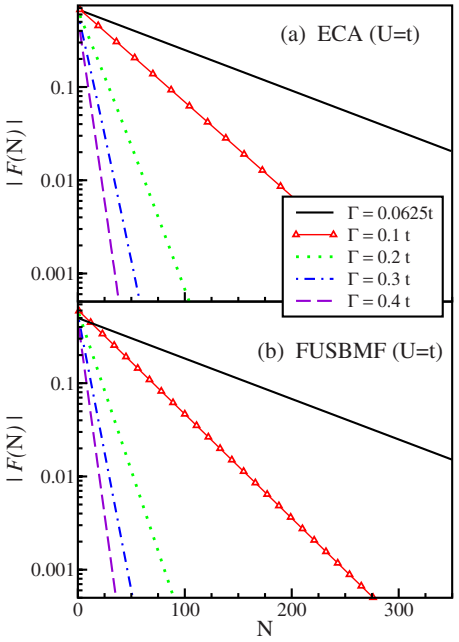

FIG. 5. (Color online) Cloud extension function $F(N)$ vs N, the site in the semichain, for several values of Γ. (a) Extrapolation to the thermodynamical limit, calculated with ECA, for each Γ value (b) same as in (a) but calculated with FUSBMF. Note that, as Γ increases, and therefore T_K increases, the extension of the Kondo cloud [measured by $R_K(N)$] decreases, reflecting the shorter range of the Kondo effect. Note also that the dependence of $|F(N)|$ with N, for all Γ values shown, is perfectly linear, clearly showing the universal Kondo physics behavior.

≤ 9). Figure 4(b) shows the values obtained this way for $R_K(L)$ as a function of $1/L$ [solid (black) dots], for the different values of L used in panel (a). A fitting of these results by a quadratic polynomial is also shown [dashed (red) curve]. The intercept of the dashed (red) curve with the vertical axis provides an extrapolation of R_K to the thermodynamical limit $R_K(L\rightarrow\infty)$. This extrapolated value of R_K can then be used in Eq. (23) to obtain the thermodynamical limit for the $|F(N)|$ curve, which, for $\Gamma/t=0.1$, is the open (red) triangles in Fig. 4(a).[29]

Obviously, Eq. (23) has two free parameters, viz., A_0 and R_K. Although the vertical axis in Fig. 4(a) is logarithmic, making it difficult to judge the convergence of A_0, it is true that A_0 converges with L faster than R_K (note that, in accordance with Eq. (23), A_0 is the y intercept and R_K is the negative of the inverse of the slope of the curves for different cluster sizes). The values of A_0 for different values of L where obtained from the fitting, of each data set in Fig. 4(a), done with Eq. (23). The dependence of A_0 on the parameters of the model will be discussed below.[30]

At this point, it is important to note that, as the cluster used in the FUSBMF and NRG calculations has a fixed size ($L=0$), there is no extrapolation to be done to find $|F(N)|$ for both methods. There is only a fitting to Eq. (23) to find R_K and A_0.

Now that we have clarified how the thermodynamical limit value for R_K is found for each method, we want to show how it varies with the parameters of the model. Figure 5(a) shows the extrapolated (ECA) $|F(N)|$ curves, for $U=1.0$ and different values of Γ [from 0.0625 (solid (black) curve] to 0.4 (dashed (magenta) curve). From the data, it is clear that R_K (the negative of the inverse of the slope) decreases with increasing values of Γ. In panel (b), the corresponding $|F(N)|$ curves obtained with FUSBMF are shown for comparison. The overall agreement between both methods is quite good. As expected, we observe that the size of the Kondo cloud (measured through the cloud extension function) increases with U/Γ. We can understand this behavior by noting that, as Γ increases (with a fixed U), T_K also increases, and R_K, as predicted by Eq. (1), decays. Finally, we want to call attention to the fact that all the curves in Fig. 5 have the same functional form, for all values of T_K, i.e., a decaying exponential, reflecting the universality of the Kondo physics.

Figure 6 shows the results obtained [open dots in panels (a), (b), and (c)] by extrapolating R_K from $|F(N)|$ for differ-

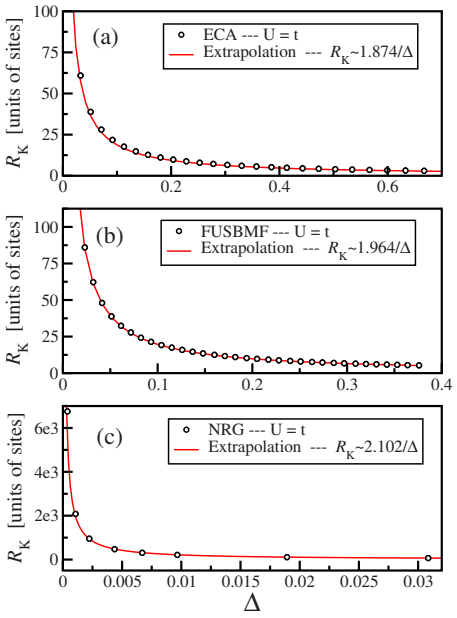

FIG. 6. (Color online) Range (R_K) of the Kondo cloud as a function of Δ. The open dots show the results obtained for R_K through the fitting of curves like the ones in Fig. 5 for various values of Δ. (a) ECA, (b) FUSBMF, and (c) NRG results. A fixed parameter $U=t$ was used for the three methods, and the parameter Γ was changed in order to obtain different Δ values. The solid (red) line in each panel shows the interpolation of an $1/\Delta$ function, as expected for R_K vs T_K (which is proportional to Δ). The value of the proportionality factor for each method is shown in the respective label.

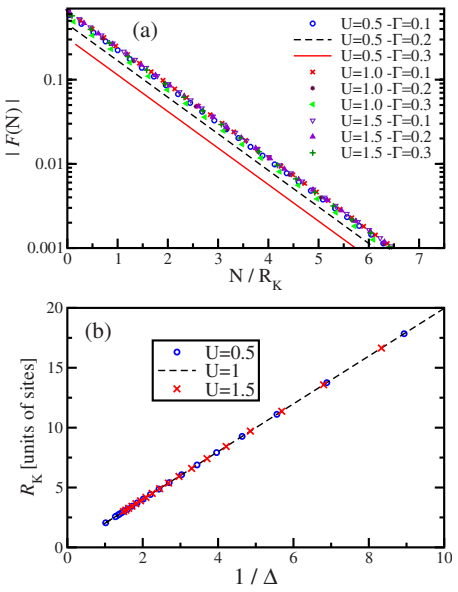

FIG. 7. (Color online) (a) Cloud extension function $F(N)$ as function of N/R_K for different values of U and Γ. Note that all the results for different values of U/Γ lay at lines with the same slope. The difference in the intercepts with the vertical axis come from different values of A_0, a fact that is explained in Fig. 8. The fixed value of the slope is due to the universality of the Kondo effect. (b) ECA results for the size of the Kondo cloud vs $1/\Delta$ for $U=0.5t$, $U=t$, and $U=1.5t$. Note that, for the interval of values of U and Γ shown, R_K is exactly a linear function of $1/\Delta$, and does not depend on the values of U and Γ used.

ent values of Γ (at $V_g=-U/2$), using (a) ECA, (b) FUSBMF, and (c) NRG. These results are plotted as a function of Δ,[31] which is taken as the full width at half height of the Kondo peak for each different value of Γ. We observe that the dependence of the Kondo length R_K with Δ satisfies the relationship given by Eq. (21) (as Δ, the width of the Kondo peak, is proportional to T_K). To emphasize that, each set of data (obtained by the three different methods) was fitted by a function $\propto 1/\Delta$ [see the solid (red) line in each panel]. It is important to stress that the proportionality coefficient between R_K and $1/\Delta$ obtained by all the three different methods is very similar, i.e., $R_K \sim 2.0/\Delta$. The proportionality factor in Eq. (21) is 1.874 for ECA, 1.964 for FUSBMF, and 2.102 for NRG. While this factor is similar for ECA and FUSBMF, there is a 10% difference between ECA and NRG. We believe that this difference comes from the parameter b used in NRG to broaden the logarithmic-Gaussian functions in the LDOS, as the value of Δ obtained by NRG is very sensitive to the choice of this arbitrary parameter.

Note the difference in the range of Δ used for the NRG calculations when compared to ECA and FUSBMF. Traditionally, NRG is a method designed to calculate the exact static properties of the Kondo problem, however it fails to provide accurate dynamical properties, such as the LDOS, away from the Fermi level. This comes from the logarithmic discretization of the band. As a consequence, mainly for larger T_K values, which are associated with broader Kondo peaks, the LDOS at the wings of the Kondo peak will be distorted enough that it will not produce good results when the EOM is applied. Due to this limitation, we compare the NRG results just with the few first points calculated using ECA and FUSBMF, which are associated with lower values of T_K. To check the universal behavior of the Kondo physics, we evaluate the cloud extension function $F(N)$ for several values of U and Γ. The results are shown in Fig. 7(a). The R_K values, used in the renormalization of N, were calculated as explained above. As expected, all the data lay at lines with the same slope, indicative of the universal behavior of $F(N)$, their different vertical intercepts being related to different values of A_0 [see Eq. (23)]. The two lines that deviate the most [solid (red) and dashed (black)] do so because they were obtained for the smaller values of U/Γ. As will be discussed in Fig. 8, for such values the system is entering in the mixed-valence regime.

Figure 7(b) shows ECA results of R_K vs $1/\Delta$ for three different values of U (0.5, 1.0, and 1.5). As shown in the figure, the functional form $R_K \propto 1/\Delta$ is valid for the intervals of U and Δ (and therefore Γ) inside which the calculations were done. More importantly, as all the curves collapse to a single line, the proportionality coefficient is also independent of these intervals. This indicate that the "propagation" of the Kondo effect into the leads (which is essentially measured by R_K) depends only on the weight of the Kondo resonance at the Fermi level (measured by Δ).

We want to stress again that the independence of R_K vs Δ with U, observed in Fig. 7(b), reflects the fact that the Kondo physics depends only upon one relevant magnitude, the

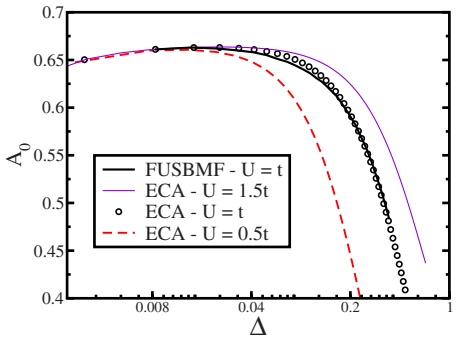

FIG. 8. (Color online) Parameter A_0 as a function of Δ (in log scale) calculated by ECA and FUSBMF. Different U, where used for ECA. Note that, when Δ is small, all curves coincide, as expected, in view of the universal behavior characteristic of a Kondo system. Increasing Δ, we enter in the mixed-valence regime, and curves for different values of U start to diverge.

Kondo temperature. In addition, one should note that, by definition, $F(N)$ is zero in the absence of interactions ($U=0$). In which case, ϱ_N^K and ϱ_N^{NK} are both exact and equal, and therefore the integrand in Eq. (22) vanishes. This implies that the behavior shown in Fig. 7(b) *is* related to many-body interactions, i.e., Kondo physics.

Figure 8 shows, for ECA and FUSBMF, the parameter A_0 as a function of Δ. We can see that, the ECA and FUSBMF curves agree quite well, for the same value $U=1.0$. Additional calculations, with different U values ($U=0.5$ and $U=1.5$), were done just with ECA. For these additional results, one sees that the curves start to differ from each other for large Δ but agree for small values ($\Delta<0.04$). The agreement for small Δ can be easily understood if one takes in account the universal behavior of the Kondo effect, in the sense that it is determined by a single energy scale, the Kondo temperature T_K. Therefore, A_0 (as R_K) does not depend on either U or Γ independently but on their ratio (U/Γ), at least until the system enters the mixed-valence regime, at higher Δ (equivalent to Γ). Notice that the curve for lower U ($U=0.5$) starts to diverge from the other two at a lower value of Δ (proportional to Γ) while the opposite occurs for the larger-U curve.[28]

V. CONCLUSIONS

Using the LDOS within the metal lead, we have estimated the effective length, in real space, of the effect of the many-body correlations originating at the impurity site. For the Kondo effect, we defined a cloud extension function $F(N)$ in order to estimate when an electron located at a site N, away from the impurity, is not affected anymore by its presence.

Indeed, we have used the electronic properties reflected in the LDOS function (*charge spectra*) of the one-dimensional metallic lead, to study the spatial propagation of the Kondo effect away from the magnetic impurity. The length of the Kondo cloud, R_K, has been defined in the literature to be the extension of the spin-screening cloud, formed by the conduction electrons, in the vicinity of the impurity. From this point of view, it is essentially the spatial size of a *magnetic* property, as it is associated to the spin-spin correlations between the local impurity and the conduction-electron spins.[13] However, here we claim that, as far as the Kondo cloud is concerned, the *charge spectra* counterpart of the Kondo physics (defined as the effect of the impurity's Kondo peak over the LDOS of the leads) is equivalent to its magnetic expression, as they are both manifestations of the same physical phenomenon. Moreover, we claim that $|F(N)|$, being dependent just on the LDOS, is easier to calculate and measure than spin-correlation-based functions.

As far as transport properties are concerned, if the Kondo effect is thought to be the way in which two or more QDs can interfere, the relevant way of studying the Kondo cloud is by analyzing the effect of the impurity over the LDOS of the rest of the system.

In order to study the spatial propagation of the Kondo effect, we define what we call a cloud extension function, denoted $F(N)$ [see Eq. (22)], and show that it is an universal function of the variable N/R_k. It measures, in an interval of width T_K around the Fermi energy, the distortion of the LDOS, at site N, created by a Kondo impurity sitting at the origin, for a one-dimensional configuration.

One important feature of $F(N)$, besides its universal character, is that, through the Lorentzian distribution, the Friedel oscillations, and its associated trivial $1/N$ dependence contained in the density, are eliminated, and just the relevant physics due to the Kondo effect survives (see Appendix).

We evaluated function $F(N)$ using three totally different formalisms, ECA, FUSBMF, and NRG, and obtained almost identical results for the variation in R_K with the parameters of the system. The fact that three different formalisms provide the same physical description makes this study quite robust and reliable. We demonstrate, as well, that the length of the Kondo cloud is controlled by the unique, scaling invariant, relevant parameter of the Kondo effect, the Kondo temperature T_K. These results permit a very accurate determination of the functional form of $R_K(T_K)$, in agreement with intuitive ideas, summarized in Eq. (1).

Recently, Holzner *et al.*, using DMRG, have calculated the spin-spin correlations involved in the formation of the Kondo cloud in a one-dimensional system. They found that the dependence of the range of the Kondo cloud with the Kondo temperature agrees with our results shown in Fig. 6.[13] We direct the reader to this reference for information on additional works that use spin-spin correlations to determine the properties of the Kondo cloud.

Finally, it is important to emphasize that the measurement of spin-spin correlations between different sites, in a real STM experiment, is difficult to perform, as the use of two different STM tips, at the same time, is required.[32] On the other hand, the mapping of the Kondo cloud through the difference in the conductance, measured by an STM tip, at different points in a 1D system, looks more feasible, as it has already been performed in metallic surfaces.[15]

ACKNOWLEDGMENTS

The authors wish to acknowledge fruitful discussions with K. A. Al-Hassanieh, G. Chiappe, E. H. Kim, and especially

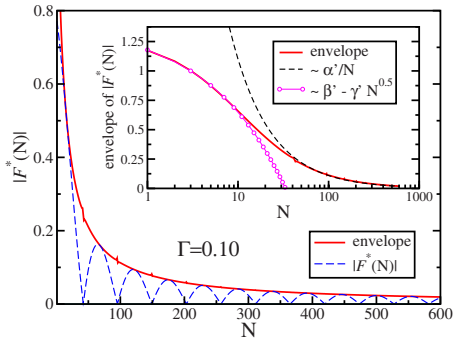

FIG. 9. (Color online) Magnitude of $F^*(N)$ as a function of N. Dashed (blue) line shows $|F^*(N)|$ vs N (Ref. 34), the solid (red) line shows the envelope function. The inset shows the envelope function and its two asymptotic limits. For large N, i.e., $R_K/N<1.0$, the envelope can be fitted by a $\propto \alpha'/N$ curve and for small N ($R_K/N>1.0$, i.e., inside the Kondo cloud), the envelope behaves as $\propto \beta' - \gamma' N^{0.5}$, where the values obtained from the fittings were $\alpha'=11.1759$, $\beta'=1.4208$, and $\gamma'=0.243$.

F. Heidrich-Meisner. E.V.A. thanks the Brazilian agencies FAPERJ, CNPq (CIAM project), and CAPES for financial support. G.B.M. and C.A.B. acknowledge support from NSF under Grant No. DMR-0710529. E.D. is supported by the NSF under Grant No. DMR-0706020 and the Division of Materials Sciences and Engineering, Office of Basic Energy Sciences, U.S. Department of Energy. E.V. acknowledges support from CNPq (CIAM project).

APPENDIX: FRIEDEL OSCILLATIONS

In this section, we discuss the effect of the Friedel oscillations in the charge density and how they are related to the extension function $F(N)$ defined in this work. Following Affleck *et al.*[8] and Bergmann,[10] the local charge per spin on site N can be defined as

$$\rho(N) = \frac{-1}{\pi}\int_{-\infty}^{\infty} f(\omega - E_F, T)\mathrm{Im}[G_{NN}(\omega)]d\omega, \qquad \text{(A1)}$$

where $f(\omega,T)$ is the Fermi distribution.

It can be shown that the difference $\rho(N)-\rho_0(N)$ in the local charge on site N, between when the impurity is present $[\rho(N)]$ and when it is not $[\rho_0(N)]$, at $T=0$, displays the so-called Friedel oscillations, with a wavelength associated to the Fermi wave vector.[8,33] In the equation above, these oscillations come from integrating the step Fermi distribution at $T=0$. Effectively, by performing the integration at finite T, the oscillations are eliminated.

The envelope of this difference (look inset of Fig. 1 in Ref. 8) presents two asymptotic regimes: (i) far away from the impurity, for electrons out of the Kondo cloud, just the Friedel oscillations remain and the envelope decays as $\propto 1/N$ (this is obtained as a direct consequence of Fermi-liquid theory). (ii) Close to the impurity, on the other hand, where the effect of the Kondo physics is relevant, the envelope function of the local charge behaves as $1-b\pi/[\ln^2(cR_K/N)]$, where b and c are constants of order 1 (this can be obtained from a weak-coupling theory).

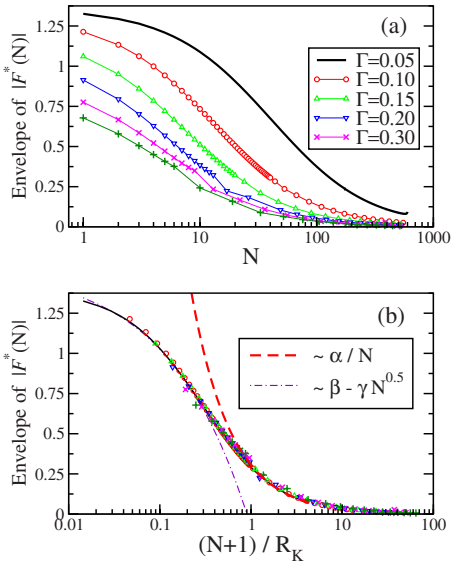

FIG. 10. (Color online) (a) Envelope of $|F^*(N)|$ calculated for different values of Γ. (b) By rescaling N as $(N+1)/R_K$ it can be shown that all the curves have the same asymptotic limit $\propto \alpha/N$ when $N>R_K$ and $\beta-\gamma N^{0.5}$ when $N<R_K$. Note that the R_K values used in the renormalization were calculated in Sec. IV through $F(N)$, i.e., including a Lorentzian distribution. The values obtained from the fittings were $\alpha=0.3059$, $\beta=1.54104$, and $\gamma=1.54104$.

To compare our results with those for the local charge, as calculated in Refs. 8 and 10, we proceed as follows. In order to obtain the Friedel oscillations, we replace the Lorentzian distribution used in Eq. (22) by a step function. We define then a new extension function as

$$F^*(N) = \int_{-\infty}^{\infty} \frac{1}{\Delta}[f_0(\omega-\Delta/2) - f_0(\omega+\Delta/2)] \times [\varrho_N^K(\omega) - \varrho_N^{NK}(\omega)]d\omega, \qquad \text{(A2)}$$

where $f_0(x)$ is the step function with value 1 for $x<0$ and 0 for $x>0$. Note that this new definition is equivalent to that in Eq. (22), as the only difference is that the Lorentzian distribution was replaced by a normalized square function of width Δ.

In Fig. 9, the magnitude of $F^*(N)$ [dashed (blue) line] for $\Gamma=0.1$ is shown.[34] First, we observe that the mere change in the function used to convolute the integral (from Lorentzian to square function) results in the appearance of the characteristic Friedel oscillations discussed previously. The envelope of this function is obtained as $F^*(N)/\sin(\lambda_0 N+\phi)$, where λ_0 and ϕ are, respectively, the characteristic wavelength and phase, obtained numerically. The solid (red) line shows the envelope obtained. In the inset, the two asymptotic regimes for this function can be observed. For large N, the function decays as $\propto 1/N$, as expected, as only the Friedel oscillations survive. At short range, close to the impurity, we find that the asymptote behaves as $\propto\sqrt{N}$, due to the nontrivial Kondo physics.

In Fig. 10(a), we show the envelope of $|F^*(N)|$ for several values of Γ. Rescaling this function, by changing the independent variable from N (site position away from the impu-

rity) to $(N+1)/R_K$ [where R_K was found as described in Sec. IV, using $F(N)$ with a Lorentzian distribution], we observe that for either long distances, i.e., *outside* the Kondo cloud, where the Friedel oscillations dominate, and *inside* the Kondo cloud, where Kondo physics dominates, the behavior of $|F^*(N)|$ is universal. This result is shown in Fig. 10(b). In the rescaling used in Fig. 10, we have translated the data by one site because that way the universality is more perfectly achieved. Although there is a certain degree of arbitrariness in setting the spatial origin of our system, we emphasize that, for the sake of our argument here, this difference is completely irrelevant in the most important region, i.e., where the crossover occurs.

In conclusion, as shown in this appendix, the Friedel oscillations can be eliminated if, instead of using the step function as defined in Eq. (A2), we use Fermi distributions with temperature T_K, where it is the smoothness of the distribution at the edges that eliminates the oscillations seen in Fig. 9 [dashed (blue) curve]. For the same reason, when we use a Lorentzian distribution, the Friedel oscillations are eliminated, and the only remaining effect, *inside* the Kondo cloud, is the one produced by the Kondo physics.

*Corresponding author; carlos.busser@gmail.com

[1] D. Goldhaber-Gordon, H. Shtrikman, D. Mahalu, D. Abusch-Magder, U. Meirav, and M. A. Kastner, Nature (London) **391**, 156 (1998).
[2] E. S. Sørensen and I. Affleck, Phys. Rev. B **53**, 9153 (1996).
[3] E. S. Sørensen and I. Affleck, Phys. Rev. Lett. **94**, 086601 (2005).
[4] H. C. Manoharan, C. P. Lutz, and D. M. Eigler, Nature (London) **403**, 512 (2000).
[5] Although one should be cautious in taking this approach, as a heavy fermion system is modeled by a Kondo lattice Hamiltonian while all the results presented here are for a single impurity.
[6] J. E. Gubernatis, J. E. Hirsch, and D. J. Scalapino, Phys. Rev. B **35**, 8478 (1987).
[7] E. S. Sørensen and I. Affleck, arXiv:cond-mat/9508030 (unpublished); V. Barzykin and I. Affleck, Phys. Rev. Lett. **76**, 4959 (1996); P. Simon and I. Affleck, *ibid.* **89**, 206602 (2002); P. Simon and I. Affleck, Phys. Rev. B **68**, 115304 (2003); K. Ingersent, A. W. W. Ludwig, and I. Affleck, Phys. Rev. Lett. **95**, 257204 (2005).
[8] I. Affleck, L. Borda, and H. Saleur, Phys. Rev. B **77**, 180404(R) (2008).
[9] G. Bergmann, Phys. Rev. B **77**, 104401 (2008); G. Bergmann, arXiv:0901.3347 (unpublished).
[10] G. Bergmann, Phys. Rev. B **78**, 195124 (2008).
[11] C. J. Gazza, M. E. Torio, and J. A. Riera, Phys. Rev. B **73**, 193108 (2006); S. Costamagna, C. J. Gazza, M. E. Torio, and J. A. Riera, *ibid.* **74**, 195103 (2006).
[12] L. Borda, Phys. Rev. B **75**, 041307(R) (2007).
[13] A. Holzner, I. McCulloch, U. Schollwöck, J. von Delft, and F. Heidrich-Meisner, arXiv:0906.2933 (unpublished).
[14] J. Simonin, arXiv:0708.3604 (unpublished).
[15] V. Madhavan, W. Chen, T. Jamneala, M. F. Crommie, and N. S. Wingreen, Science **280**, 567 (1998).
[16] V. Ferrari, G. Chiappe, E. V. Anda, and M. A. Davidovich, Phys. Rev. Lett. **82**, 5088 (1999); C. A. Büsser, E. V. Anda, A. L. Lima, M. A. Davidovich, and G. Chiappe, Phys. Rev. B **62**, 9907 (2000); G. B. Martins, C. A. Büsser, K. A. Al-Hassanieh, E. V. Anda, A. Moreo, and E. Dagotto, Phys. Rev. Lett. **96**, 066802 (2006).
[17] C. A. Büsser, G. B. Martins, K. A. Al-Hassanieh, A. Moreo, and E. Dagotto, Phys. Rev. B **70**, 245303 (2004); E. V. Anda, G. Chiappe, C. A. Büsser, M. A. Davidovich, G. B. Martins, F. Heidrich-Meisner, and E. Dagotto, *ibid.* **78**, 085308 (2008).
[18] G. Kotliar and A. E. Ruckenstein, Phys. Rev. Lett. **57**, 1362 (1986).
[19] D. M. Newns and N. Reed, Adv. Phys. **36**, 799 (1987).
[20] K. G. Wilson, Rev. Mod. Phys. **47**, 773 (1975).
[21] E. Dagotto, Rev. Mod. Phys. **66**, 763 (1994).
[22] H. R. Krishna-murthy, J. W. Wilkins, and K. G. Wilson, Phys. Rev. B **21**, 1003 (1980); **21**, 1044 (1980).
[23] R. Bulla, T. A. Costi, and T. Pruschke, Rev. Mod. Phys. **80**, 395 (2008).
[24] K. Chen and C. Jayaprakash, Phys. Rev. B **52**, 14436 (1995).
[25] D. N. Zubarev, Usp. Fiziol. Nauk **71**, 71 (1960) [Sov. Phys. Usp. **3**, 320 (1960)].
[26] J. Hubbard, Proc. R. Soc. London, Ser. A **276**, 238 (1963). Another possibility for a non-Kondo solution consists in decoupling the impurity from the semichain by making $t'=0$. Our calculations were done both ways, i.e., Hubbard-I and $t'=0$, and we found agreement between the two results for the extension of the Kondo cloud R_K.
[27] It is important to comment that, the same analytic calculation performed in Ref. 8, which led to the functional forms used to fit the weak- and strong-coupling numerical data in their Fig. 1, can also be done here (although it is certainly a more involved derivation). However, the authors decided not to do so, in order to shorten the Appendix. This will be done in a forthcoming work.
[28] Note that A_0 was not calculated as $|F(0)|$ but through the fittings discussed in Figs. 4 and 5. Therefore, its value and its dependency with Δ, as seen in Fig. 8, do not represent the value or the variation in the area of the Kondo peak.
[29] A second extrapolation method can also be used (although not as accurate as the one described in Sec. IV): one can extrapolate the value of $|F(N)|$ to the thermodynamical limit $(1/L \to 0)$ for *each* value of N, and then obtain R_K by fitting the extrapolated $|F(N)|$ to Eq. (23). Although there is good qualitative agreement on the values obtained for R_K between the two extrapolation methods, we favor the first one, as it involves much less computational effort and is therefore more accurate.
[30] The limit in which $|F(N)| \to 0$ determines the order of magnitude of the Kondo cloud. However, the actual values and functional variation in both A_0 and R_K in Eq. (23) clearly indicate that R_K has a leading contribution in determining the size of the Kondo cloud, given the small variation in A_0 in the region of parameter space associated to the Kondo effect (compare the scales of the vertical axis in Figs. 6 and 8).

[31] Note that, in ECA, Δ was calculated as the thermodynamical limit $1/L \to 0$ of the width of the Kondo resonance at the impurity's LDOS.
[32] M. Ternes (private communication).
[33] F. Mezei and G. Grüner, Phys. Rev. Lett. **29**, 1465 (1972).
[34] Note that, in the dashed (blue) curve, the site to site oscillations [similar to the ones displayed in the inset of Fig. 4(a)] were removed, to improve clarity and emphasize the oscillating behavior of $|F^*(N)|$.